

Efficient GHz electro-optical modulation with a nonlocal lithium niobate metasurface in the linear and nonlinear regime

Agostino Di Francescantonio¹, Alessandra Sabatti², Helena Weigand², Elise Bailly², Maria Antonietta Vincenti³, Luca Carletti³, Jost Kellner², Attilio Zilli¹, Marco Finazzi¹, Michele Celebrano¹, and Rachel Grange²

¹ Politecnico di Milano, Physics Department, Milano, Italy

² ETH Zürich, Department of Physics, Institute for Quantum Electronics, Optical Nanomaterial Group, 8093 Zürich, Switzerland

³ Università di Brescia, Department of Information Engineering, Brescia, Italy

Abstract

Electro-optical modulation is widely employed for optical signal processing and in laser technology. To date, it is efficiently realized in integrated photonic systems as well as in bulk optics devices. Yet, the achievement of modulators exploiting Pockels effect in flat optics, essential to scale down the electric radiation-optical control in free space, currently lag behind bulk and on-chip integrated platforms in terms efficiency and speed. We bridge this gap realizing a metasurface based on lithium niobate (LiNbO₃) on insulator that leverages on resonances with quality-factor as high as $8 \cdot 10^3$ to achieve fast electrical modulation of both linear and nonlinear optical properties. LiNbO₃, well known for its high nonlinear susceptibility and wide transparency window across the infrared and visible spectrum, is employed to realize an asymmetric, one-dimensional array of nanowires, exhibiting resonances with linewidth < 0.2 nm. By applying a CMOS-compatible electrical bias, the metasurface imparts a relative reflectivity modulation around 0.1, with a modulation efficiency, defined as relative modulation *per* applied Volt, larger than 0.01 V^{-1} on a bandwidth of about 1 GHz. We also demonstrated more than one order of magnitude intensity modulation of the second harmonic seeded by a continuous-wave laser, with a modulation efficiency of about 0.12 V^{-1} . This dual modulation capability, rooted in the interplay between optical resonances and electric field manipulation, holds significant potential for cutting-edge applications in high-speed photonics, nonlinear optics, and reconfigurable communication systems. Our findings highlight the transformative potential of LiNbO₃-based metasurfaces for integration into next-generation optical technologies that demand rapid, efficient electrical control of light.

Introduction

Optical metasurfaces represent a groundbreaking platform for scaling optical components down to the micrometer thickness [1]. While most of the demonstrated optical operations rely on passive metasurfaces, whose functionalities are not tunable after fabrication, applications like beam steering, LiDAR, and free-space optical communication demand active control over various light properties, including amplitude, phase, polarization, and directionality. As a result, there is a growing emphasis on the development of reconfigurable metasurfaces aimed at creating ultra-compact free-space photonic devices capable of dynamically adjusting these essential parameters [2]. Several physical mechanisms have been explored to achieve this goal, including metasurfaces integrated with liquid crystals [3], phase-change materials [4], thermo-optic control [5][6], electro-optic (EO) modulation [7][8] as well as all-optical modulation by means of absorption of femtosecond lasers pulses [9][10], and interferometric control [11]. Although several of these approaches are very suggestive, EOM remains the most promising in terms of applications due to its compatibility with CMOS-based platforms. EOM relies on nonlinear effects, like the Pockels (or linear electro-optic) effect and the Kerr (or quadratic electro-optic) effect. Both effects result in a change of the refractive index n , induced by a static or low frequency electric field. In the case of the Pockels effect, this change is linear with respect to the quasi-static electric field, $\Delta n = -\frac{1}{2}n^3r_{\text{eff}}E_{\text{EO}}$ [12], where r_{eff} is the material effective electro-optic coefficient,

and E_{EO} is the amplitude of the driving electric field. A key advantage of the Pockels effect is its ability to achieve modulation speeds more than a hundred of GHz [13][14], with the effective observed modulation bandwidth primarily limited by the electrical design of the device actuation system. This makes the Pockels effect particularly promising for high-speed applications, such as optical communications.

Among the available material platforms, Lithium Niobate (LiNbO_3) in crystalline form is already widely used for bulk photonics devices [15], thanks to its wide transparency window from the mid-infrared to ultraviolet and its large electro-optic coefficient ($r_{33} \approx 35$ pm/V [16]) and second-order nonlinear coefficient ($d_{33} \approx -27$ pm/V [17]). Several important applications of LiNbO_3 are based on its optical nonlinearity, like EOM or frequency conversion via optical harmonic generation, such as second-harmonic generation (SHG), or spontaneous parametric down conversion. Advances in fabrication techniques have made thin-film LiNbO_3 available for integrated [18] and metasurface-based photonic devices [19]. Yet, in contrast to on-chip modulators based on LiNbO_3 waveguides, which routinely achieve efficient modulation up to the GHz range [20][14][21], the development of efficient free-space electro-optic modulators based on subwavelength platforms remains an open challenge. This can be primarily ascribed to the inherently short interaction lengths and the modest refractive index changes associated with typical electro-optic materials.

Recent efforts to expand the materials palette for EOM free-space platforms include, for example, Barium Titanate (BTO), which has been investigated as an electro-optic bottom-up metasurface [22]. However, the potential benefits of its large electro-optic coefficient ($r_{\text{BTO}} = 148$ pm/V) are hindered by non-standard fabrication techniques and by its variability depending on the specific method [23]. Alternative approaches, such as electro-optic polymers, while exhibiting large coefficients, lack robustness for applications like automotive or under high laser exposure [24]. As a result, LiNbO_3 is still the most reliable material for electro-optic modulation, owing to its remarkable nonlinear optical properties and established top-down fabrication processes.

Metasurfaces offer a viable route to maximize the effects associated with refractive index modulation [25], thanks to enhanced light-matter interactions. In particular, nonlocal metasurfaces, characterized by spectrally sharp resonances such as lattice resonances [26], guided mode resonances (GMRs) [27], and bound states in the continuum (BICs) [28][29], are extensively investigated as potential free-space modulators. Recently, Benea-Chelmus et al.[8] demonstrated, for the first time, free-space GHz modulation from a Si metasurface supporting BICs and GMRs embedded in an organic, electro-optic layer. However, achieving a modulation efficiency greater than 10^{-2} with CMOS-compatible voltages (up to 5 V) remains a non-trivial task. This challenge is further complicated by the requirement to realize high-quality factor (Q) structures and to couple them effectively to free-space radiation [28]. In addition to boosting the quality factor of optical resonances, modulation efficiency can be also improved by optimizing the static electric field distribution E_{EO} by means of specific electrode designs, although this often comes at the expense of a reduced device bandwidth [30][26].

In this study, we introduce and demonstrate a groundbreaking use of nonlocal metasurfaces based on monolithic lithium niobate on insulator (LNOI) platform. By leveraging a high-quality factor resonance, we achieve efficient intensity modulation of free-space signals within the telecom C band. Our experimental results reveal a modulation efficiency exceeding 10 %, driven by less than 10 V and an operational bandwidth of about 1 GHz. Beyond linear signal modulation, our system also effectively modulates nonlinear upconverted signals, namely SHG. Notably, we find that the second harmonic signal exhibit significantly larger modulation compared to linear signals, as the nonlinear response originates directly from the material itself. Moreover, the squared dependence of the SHG on the fundamental field enhances the sensitivity to variations in the resonant properties of the system [31]. By harnessing the nonlinear characteristics of lithium niobate, we demonstrate electro-optic modulation of SHG excited by a continuous-wave (CW) pump laser, achieving a striking 110 % intensity

modulation. This advancement paves the way for the development of a novel class of modulators for upconverted signals, offering exciting possibilities for future photonic technologies.

Design and linear characterization

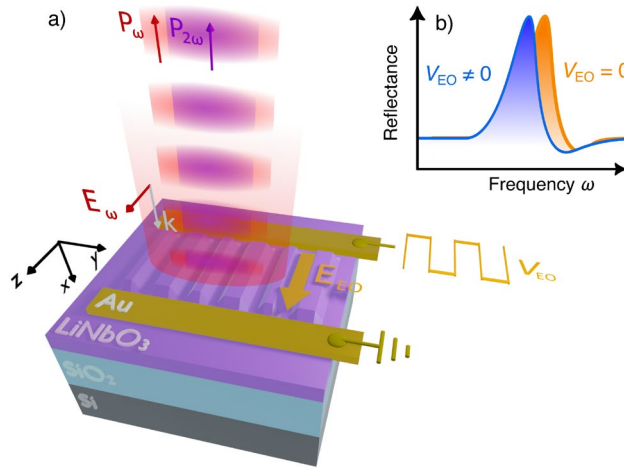


Figure 1. Linear and nonlinear electro-optic modulation. a) Sketch of modulated reflected power of a beam at fundamental frequency P_ω and of its second harmonic $P_{2\omega}$ from a x-cut LiNbO₃ on a SiO₂-Si substrate. The modulation is induced by an applied voltage (V_{EO}), which produces a driving electric field E_{EO} parallel to the optical field E_ω . b) Illustration of a resonance shift induced by electro-optic effect.

Figure 1 illustrates the design and working principle of our device. We investigate a nonlocal lithium niobate on insulator (LNOI) metasurface made by asymmetric, periodically arranged nanostripes obtained from an x-cut LiNbO₃ thin film on a finite SiO₂ layer on top of a Si substrate (Figure 1a). We aim at observing efficient and fast electric modulation of the metasurface optical properties induced by a control voltage, V_{EO} applied to the metasurface. To this aim, in-plane, gold contacts generate an electric field (E_{EO}) aligned along the z-axis to exploit the largest component of the electro-optic tensor r_{33} of LiNbO₃. To obtain a significant intensity modulation, the structure must sustain resonant modes, which are spectrally shifted when the refractive index is modulated by an applied voltage (Figure 1b). Furthermore, at a given wavelength λ_0 , a device with large quality factor $Q = \lambda_0 / \delta\lambda_0$ features a resonance with a narrow spectral width $\delta\lambda_0$ and, consequently, a large sensitivity to small variations of the refractive index induced by the applied voltage.

To this aim, we exploit high Q resonances hosted by a dielectric waveguide slab – namely, a high refractive index layer (LiNbO₃), comprised between two low-index claddings (air and SiO₂) – patterned with a diffraction grating (periodically arranged nanowires) [32]. A planar dielectric waveguide is known to host guided modes whose dispersion lies below the light line, fully confining the radiation in the slab volume with no access from external radiation sources. The reduction of translational symmetry introduced by the grating causes a folding of the guided modes dispersion in the first Brillouin zone, ending up above the light line, and consequently evolving in optically accessible guided mode resonances (GMRs) [33][34]. A mirror symmetry of the grating with respect to the xz plane yields a dark fundamental mode at the Γ point (i.e., at normal incidence) due to the odd electric field distribution (see Figure 2d), namely becoming a symmetry-protected BIC. By introducing a small asymmetry in the nanowires' widths, we further reduce the translational symmetry of the system, turning the BIC into a leaky, quasi-BIC with finite Q (see Figure 2e), which can now be excited at the Γ point.

The design optimization has been performed initially by means of rigorous coupled-wave analysis, typically applied to solve scattering from periodic dielectric structures [35]. The EO effect and the SHG

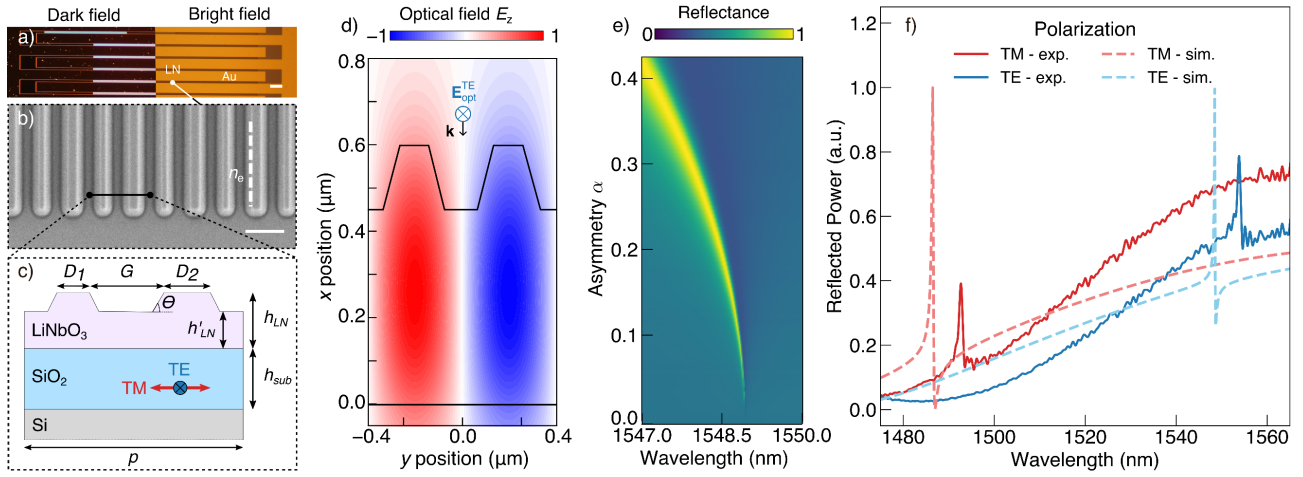


Figure 2 Sample layout and linear optical characterization. **a)** Dark field and bright-field images in real colours of the LiNbO₃ chip. The LiNbO₃ metasurfaces are located in the areas with strong scattering (bright areas in dark field). The horizontal white bar on the bottom-right sets the scale to 100 μm . The orange lines identify the edges of the interdigitated electrodes, which are fully visible in the bright field image. **b)** Scanning-electron micrograph showing the metasurface obtained by patterning the LiNbO₃ thin film. The solid horizontal bar on the bottom-right sets the scale to 500 nm. The white, dashed line defines indicates the LiNbO₃ extraordinary axis. **c)** Schematic of the cross-sectional view of a single unit cell of the array, taken by cutting orthogonally to the grooves (see black, solid line panel b), with labels corresponding to the main geometrical parameters. All the samples have the same periodicity $p = 800$ nm and LiNbO₃ height before ($h_{\text{LN}} = 600$ nm) and after patterning ($h'_{\text{LN}} = 450$ nm) ($h_{\text{sub}} = 2$ μm). The angle $\theta = 65^\circ$ accounts for the sidewall slopes introduced by the physical etching. Parameters that vary from sample to sample are the filling factor $FF = 1 - (D_1 + D_2)/p$ and the asymmetry parameter $\alpha = (D_2 - D_1)/(D_2 + D_1)$. Red and blue arrows indicate the polarization of the incident wave that excites the TM (parallel to the LN ordinary axis) and or TE (parallel or perpendicular to the LN extraordinary axis) mode, respectively. **d)** COMSOL simulation of the optical field z-component of the optical field \mathbf{E}_{opt} , excited at the quasi-BIC resonance for $FF = 0.3$ and $\alpha = 0$. Incident optical field \mathbf{E}_{opt} is TE-polarized and propagates with $\mathbf{k} \parallel (-x)$. **e)** COMSOL plane-wave simulation of the metasurface reflectance depending on the asymmetry parameter α , with fixed $FF = 0.3$. **f)** Normalized reflection spectra of the sample with $FF = 0.3$ and $\alpha = 0.19$. Solid lines show experimental data obtained by sweeping the laser wavelength in steps of 10 pm, with electric field exciting the TE mode. Dashed are the corresponding COMSOL numerical simulations.

are then modelled with a finite-element commercial software (COMSOL Multiphysics®, see Methods). The main geometrical parameters are sketched in Figure 2c. By setting the unit cell periodicity as $p = 800$ nm, the metasurface features the fundamental TE₂₁ resonant mode at the Γ point in the communication C band (i.e., 1530 to 1565 nm). This mode shows up in the reflectance spectrum when the structure asymmetry $\alpha = (D_2 - D_1)/(D_2 + D_1)$ is nonzero, with a linewidth broadening with increasing α (see Figure 2e) [36]. We set D_1 and D_2 to have a fill factor $FF = 1 - (D_1 + D_2)/p = 0.3$, corresponding to a fundamental TE mode around 1550 nm, and $\alpha = 0.2$, to realize a theoretical $Q = 11000$. Such a value for the Q factor is selected since it allows more tolerance in terms of fabrication accuracy and better resonance coupling in the experiment. Nevertheless, Q is sufficiently high to achieve efficient EO modulation, since the associated mode linewidth ($\delta\lambda_0 \approx 0.15$ nm), is comparable with the expected EO shift induced by CMOS compatible voltages, assuming a tuning sensitivity $\Delta\lambda_{\text{EO}}/\Delta V_{\text{EO}} \approx 0.01$ nm/V [26][28].

The metasurfaces were realized on a commercial LNOI stack with 600 nm-thick LiNbO₃ film on top of a SiO₂ layer with thickness $h_{\text{sub}} = 2$ μm (see Figure 2a,b,c) following a top-down approach (see Methods and Ref. [37]). The choice of planar Au electrodes ensures a uniform distribution of the driving electric field in the LiNbO₃ film, which increases the overlap with the field of the optical mode, also located mostly in the LiNbO₃ volume (Figure 2d). The uniform electric field distribution is advantageous for electro-optic (EO) modulation, as effectively leveraging the Pockels effect depends on the overlap between the low-frequency electric field and the optical field within the LiNbO₃ material. We realized a set of replicas with slight variation of D_1 and D_2 (see Methods for details) to target the sample geometry

closer to the desired quality factor and resonance position, finally identifying a fabricated replica with $\alpha = 0.19$ and $FF = 0.3$ as the one matching the original design specifications.

The linear properties and the EO response of the sample are characterized in an epi-reflection configuration by impinging with a linearly polarized, continuous-wave (CW) diode laser tuneable in the optical communication C band (1460 nm – 1570 nm) and detecting the reflected signal with a photodiode (details in Methods). The quasi-BIC resonance wavelength shifts when interrogated away from the Γ point of the photonic band structure, typically by about 10 nm/deg. Therefore, to mitigate the resonance linewidth broadening resulting from the angular spread of the light from the objective, we use a cylindrical lens to focus the excitation beam onto the objective back-aperture. This approach effectively reduces the numerical aperture, enabling nearly collimated illumination in the direction of the nonlocal mode extension. At the same time, due to the one-dimensional character of the metasurface, we tightly focus the beam on the direction parallel to the nanowires, hence preserving a sizeable beam fluence. We determine the resonance position by sweeping the laser wavelength, obtaining the reflectance spectra depicted in Figure 2f. The sharp quasi-BIC peak is superimposed to a broad Fabry–Pérot fringe caused by the 2 μm -thick SiO_2 layer. A polarization parallel or perpendicular with respect to the LiNbO_3 extraordinary index n_e excites either a transverse-electric (TE) or transverse-magnetic (TM) mode, respectively, resulting in a reflection peak at 1553 nm or 1492 nm, respectively. We also report an experimental redshift of about 5 nm with respect to the COMSOL finite-element simulations of the same structures (see Figure 2f). This slight discrepancy could be attributed to fabrication tolerances.

We investigate the static EO response of the device by applying a bias $V_{\text{EO}} = V_{\text{DC}}$ by means of a waveform generator. The shift of the quasi-BIC resonance can be clearly identified in the reflectance spectra of Figure 3a, superimposed to an unmodulated instrumental artifact. Due to the asymmetry in the resonance lineshape arising from the interaction between the sharp quasi-BIC and the broad Fabry–Pérot fringe, we fitted the experimental data using a Fano profile [38]. From the retrieved central wavelength λ_0 we estimate an EO induced shift of about $\Delta\lambda_{\text{EO}} \approx 0.05$ nm when $\Delta V_{\text{DC}} = 9$ V, close to the value retrieved from the simulated spectra in Figure 3b ($\Delta\lambda_{\text{EO}}^{\text{sim}} \approx 0.06$ nm). We, therefore, estimate a device tuning sensitivity $\Delta\lambda_{\text{EO}}/\Delta V_{\text{EO}} = 5.6$ pm/V. We also evaluate the resonance quality factor to be $Q_{\text{exp}} > 8000$, where $\delta\lambda_0^{\text{exp}} = 0.18$ nm is the resonance linewidth retrieved by the fitting. This result is in good agreement with the value calculated from the simulations ($Q_{\text{sim}} \approx 11000$ with $\delta\lambda_0^{\text{sim}} = 0.15$ nm, see Figure 3b). The lower value of the measured quality factor with respect to the simulated one might be related to fabrication imperfections and to the inherent difference in the excitation scheme between the simulated platform (perfectly planar wavefront) and the real system (partially collimated beam).

To observe the dynamic modulation of the reflectance, we apply a sinusoidal driving potential $V_{\text{EO}}(t) = \frac{V_{\text{pp}}}{2} \sin(2\pi f_{\text{mod}} t)$, characterized by a variable peak-to-peak amplitude V_{pp} and modulation frequency f_{mod} . We use a lock-in amplifier, referenced by the same waveform generator, to demodulate at $f = f_{\text{mod}}$, obtaining the signal oscillation amplitude $P_\omega(f = f_{\text{mod}})$. The DC component of the signal $P_\omega(f = 0)$ (namely, the reflectance) is synchronously detected in order to track modulation efficiency variations while changing excitation wavelength. We modulate the signal at $f_{\text{mod}} = 100$ kHz, well below the cutoff of our detection system (600 MHz). The relative modulation is calculated by evaluating the ratio $P_\omega(f = f_{\text{mod}})/P_\omega(f = 0)$, which corresponds to $\Delta P_\omega/P_\omega = (P_\omega(V = V_{\text{pp}}/2) - P_\omega(V = 0))/P_\omega(V = 0)$. The dispersive nature of the reflection spectrum will cause a dependence on λ of the modulation amplitude, which is maximized by exciting at the resonance derivative extrema. The maximum modulation amplitude that is obtained from the data

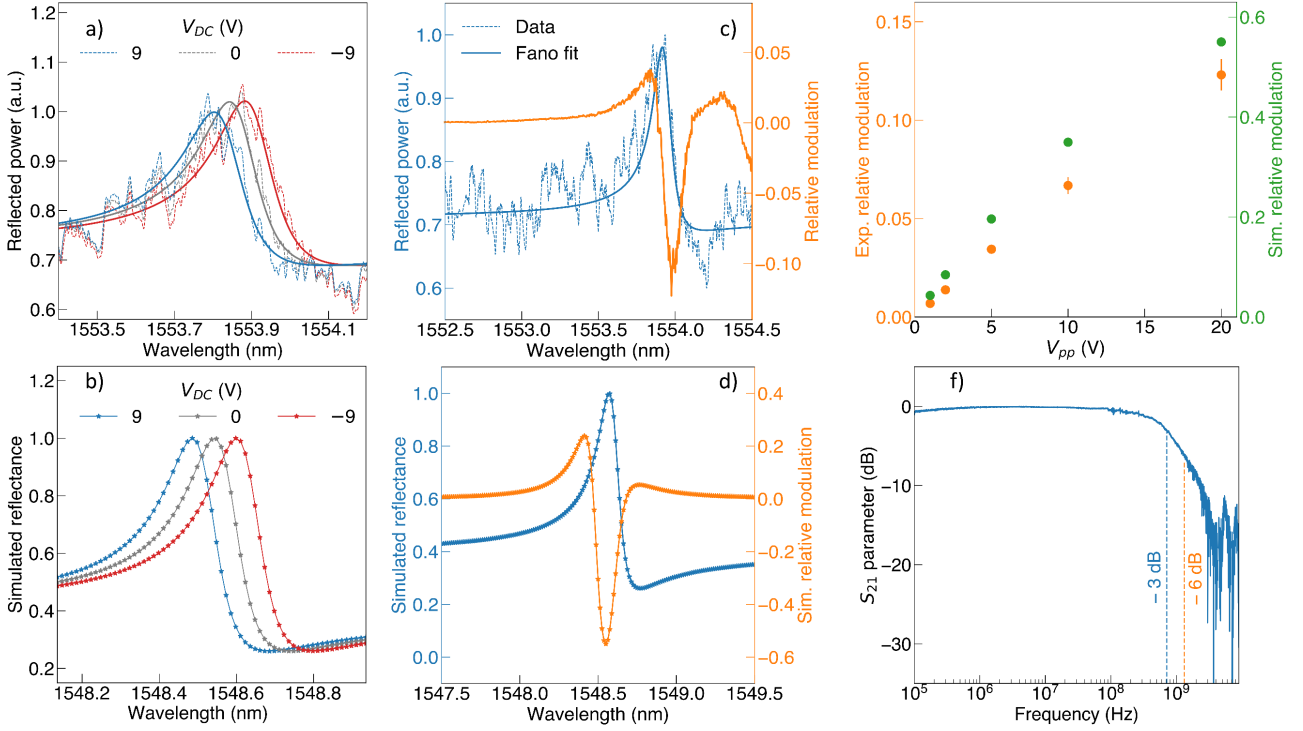


Figure 3. Characterization of the reflected signal modulation by applying DC and AC electrical stimuli. **a)** Resonance shift upon driving the metasurface with a static bias V_{DC} . The dashed lines correspond to the reflected intensity for three different values of V_{DC} , the solid lines are obtained by fitting the data with a Fano profile. **b)** COMSOL finite-element simulations of the reflectance for different applied V_{DC} values. **c)** Relative modulation (in orange), defined as the ratio $P_{\omega}(f = f_{mod})/P_{\omega}(f = 0)$, where $P_{\omega}(f = f_{mod})$ is the signal demodulated at the modulation frequency f_{mod} and $P_{\omega}(f = 0)$ is the DC component of the signal, corresponding to the reflectance. The sinusoidal driving field is characterized by a peak-to-peak amplitude $V_{pp} = 20$ V and a frequency $f_{mod} = 100$ kHz. The bias V_{DC} is set to 0. In blue, the reflectance spectrum (dashed) and its Fano profile fit (solid). The wavelength is swept by steps of 10 pm. **d)** Simulated reflectance spectrum and relative modulation (orange dots), calculated as $(P_{\omega}(V = V_{pp}/2) - P_{\omega}(V = 0))/P_{\omega}(V = 0)$, with $V_{pp} = 20$ V. **e)** Experimental (orange) and simulated (in green) variation of the maximum modulation with respect to the peak-to-peak modulating amplitude V_{pp} . Experimental points are obtained by modulating with $f_{mod} = 100$ kHz. **f)** Device frequency response obtained by calculating the parameter $S_{21} = 10 \log_{10}(P_{\omega}(f)/P_{\omega}^{max}(f))$ with a vector-network analyzer (VNA). The VNA oscillator drives the sample with $V_{pp} = 1.5$ V. All the panels refer to theoretical and experimental investigations on the sample with $FF = 0.3$ and $\alpha = 0.19$. The optical field is polarized along the z axis (see Figure 2).

in Figure 3c is $\Delta P_{\omega}/P_{\omega} \cong 0.12$ (i.e., 0.24 of peak-to-peak relative modulation), obtained with an input voltage as low as $V_{pp} = 20$ V. This is approximately 5 times smaller than the value obtained from simulations (see Figure 3d). Such a discrepancy is mostly due to the high level of unmodulated reflectance in the spectrum that is not captured by the simulations. Figure 3e illustrates how electro-optically induced modulation varies with V_{pp} . At low modulating amplitudes $\Delta\lambda_{EO} \ll \delta\lambda$ and η remains linear with respect to V_{pp} . In this regime, the modulation is proportional to the local derivative of the reflectance spectrum, and the linearity of Δn with respect to E_{EO} implies the linearity of η versus V_{pp} [25]. In this regime, we reach a modulation efficiency – defined as relative modulation *per* applied Volt – $\eta = \left(\frac{\Delta P_{\omega}}{P_{\omega}}\right) / \left(\frac{V_{pp}}{2}\right)$ of about 0.015 V^{-1} for $V_{pp} < 10$ V. With a larger bias, $\Delta\lambda_{EO}$ is no longer negligible with respect to the resonance width, resulting in a deviation from linearity. We point out that the investigation shows a modulation amplitude of the order of 0.07 for a CMOS technology-compatible voltage ($V_{pp} = 10$ V). Similar efficiency was reported in the literature only from devices sacrificing the modulation bandwidth to attain larger E_{EO} [26]. We performed the analysis of the modulation efficiency on several fabricated designs, always obtaining values between 0.05 and 0.1 for $V_{pp} = 10$ V. To complete the investigation, we studied the efficiency of the TM mode, obtaining a reduced modulation depth caused

both by the smaller electro-optic coefficient $r_{13} = 10.3 \text{ pm/V}$ [16] and by the slightly larger resonance width of 0.5 nm.

Finally, we characterized the modulation speed of the device. To overcome the limitation set by the lock-in amplifier bandwidth (600 MHz), we employed a vector-network analyzer (VNA) operating at frequencies up to 20 GHz and delivering a bias peak-to-peak amplitude $V_{pp} = 1.5 \text{ V}$. Figure 3f displays the resulting VNA transmission parameter, defined as $S_{21} = 10 \log_{10}(P_{\omega}(f)/P_{\omega}^{\max}(f))$, where $P_{\omega}(f)$ is the AC component of the modulated optical signal and $P_{\omega}^{\max}(f)$ is its maximum value in the considered frequency range. We show a -3dB (-6dB) attenuation for a driving frequency $f_{-3\text{dB}} \simeq 800 \text{ MHz}$ ($f_{-6\text{dB}} \simeq 1.4 \text{ GHz}$). Possibly, a larger bandwidth could be obtained by reducing the length of the interdigitated electrodes, which is currently 1.5 mm, since their capacitance scales linearly with the length. The limit for the increased frequency will be imposed by a trade-off between the electrode length and the metasurface area, which needs a minimal size to sustain high Q optical resonances due to the nonlocal character of the mode.

SHG modulation

The observed modulation shown in the previous section is inherently limited by the imbalance between the high reflected power $P_{\omega}(V = 0)$ and the effective modulated power $\Delta P_{\omega}(\Delta V = V_{pp}/2)$. This imposes a natural upper limit on the modulation amplitude, governed by the intrinsic resonance depth, which corresponds to the ratio between the maximum and the minimum values of the Fano profile over the background. For example, considering the measured reflectance spectrum shown in Figure 3c, the maximum modulation achievable by a complete shift from the resonance peak P_{ω}^{\max} to off-resonance P_{ω}^{off} would yield $(P_{\omega}^{\max} - P_{\omega}^{\text{off}}) / P_{\omega}^{\max} \simeq 0.3$.

An advantage of modulating resonantly enhanced upconverted signals, such as SHG, is the increased sensitivity due to the quadratic dependence on the fundamental electric field resulting in narrower linewidths. However, a significant drawback is the relatively low absolute conversion efficiency arising from the perturbative nature of the nonlinear process and the small interaction volume, inherent to subwavelength devices. To generate substantial SH signals typically requires high peak intensities and, therefore, pulsed lasers. Yet, the broad bandwidths associated with pulsed sources often exceed the resonance wavelength shift $\Delta\lambda_{\text{EO}}$ achievable in ultrathin devices, making efficient EO modulation of upconverted signals a challenging task. As a result, very large bias voltages are typically required, which are incompatible with CMOS integration [39]. This limitation can only be circumvented by exploiting laser sources with linewidths significantly narrower than $\Delta\lambda_{\text{EO}}$, combined with high- Q resonances. Recently, Anthur et al. [40] demonstrated in a III-V semiconducting metasurface that the field enhancements associated with the narrow resonances of quasi-BIC modes allows one to compensate for the reduced peak intensity, hence enabling sizeable SHG even with continuous-wave (CW) pump sources.

For this reason, we employed the same tuneable CW source used for the linear characterization also as pump for the SHG. We set the laser polarization along the largest component of the $\chi^{(2)}$ tensor d_{33} , corresponding to TE illumination. The generated nonlinear signal is then spectrally filtered and detected by means of a dispersive spectrometer equipped with a charge-coupled device (CCD). We characterize the SH signal as a function of the wavelength of the pump, with a pumping intensity of 12 kW/cm^2 (see Figure 4b).

The data reveal a full width at half maximum of the SHG excitation spectrum of $\delta\lambda_{\text{SHG}} = 0.14 \text{ nm} \simeq \frac{\delta\lambda_0^{\text{exp}}}{\sqrt{2}}$. The SHG peak aligns with the maximum of the electromagnetic energy stored in LiNbO_3 , which notably does not correspond to the maximum of the reflectance spectrum shown in Figure 4a due to

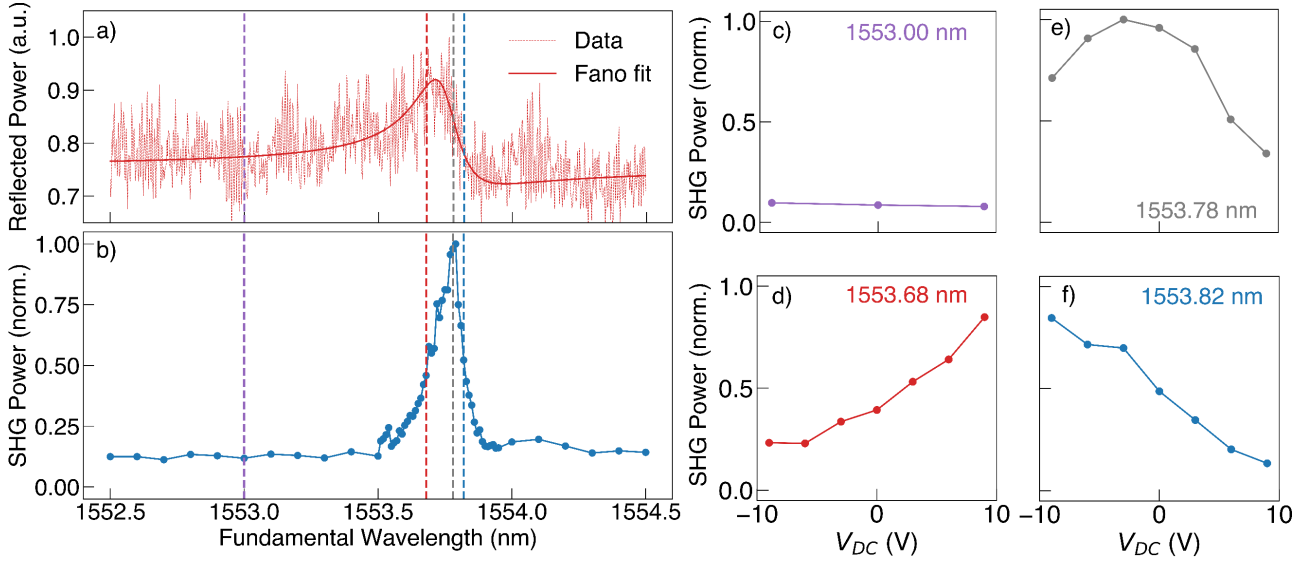


Figure 4. a) Spectrum of the reflected signal from the sample with $FF = 0.3$ and $\alpha = 0$. b) Normalized SHG excitation spectrum, obtained by sweeping the wavelength of the fundamental beam with a constant optical intensity on the sample of 12 kW/cm^2 . c–f) EO modulation of SHG, excited with four different wavelengths (identified by vertical dashed lines in panels a, b) depending on the applied DC voltage V_{DC} .

the asymmetry in the Fano lineshape. To tune the SHG emission *via* the Pockels effect, we selected various excitation wavelengths (represented by vertical, dashed lines in Figure 4b, corresponding to the SHG peak, its inflection points, and to off-resonant excitation), while varying the applied static voltage V_{DC} . In case of on-resonance pumping (as in Figure 4e) we report a reduction up to a factor of 5 upon application of $\Delta V_{DC} = \pm 9 \text{ V}$. The change in intensity becomes monotonic when the excitation is tuned on the slopes of the SHG peak (Figure 4d,f), with $(P_{SHG}(9 \text{ V}) - P_{SHG}(0 \text{ V}))/P_{SHG}(0 \text{ V}) > 1.1$ of relative SHG intensity variation by applying $\Delta V_{DC} = 9 \text{ V}$, which is in good agreement with the nonlinear simulation under same excitation conditions (a factor 2 higher). Notably, we reach a modulation efficiency $\eta = \frac{\Delta P_{SHG}}{P_{SHG}} / \Delta V_{DC} > 0.12 \text{ V}^{-1}$. The opposing trends shown in Figure 4d,f with respect to the sign of V_{DC} confirms the genuine electro-optic origin of the change in the SHG power (namely, $V_{DC} > 0 \text{ V}$ leads to a blue-shift of the resonance, enhancing/suppressing the SHG when excited on the rising/falling slope of the SHG excitation spectrum, respectively). Off-resonant excitation, on the other hand, shows low SHG signal intensity and no electro-optic modulation thereof (Figure 4c). Importantly, the low SHG signal outside the resonance leads to a high modulation efficiency, close to the simulated value. This is in striking contrast with the linear case, where the modulation is limited by a large reflectance baseline. We note that the maximum modulation that could be obtained with a complete shift of the resonance is only limited by a non-zero off-resonant SHG contribution.

Conclusion

We demonstrate a Lithium Niobate on Insulator metasurface hosting quasi-BIC resonances for high-speed, efficient EO modulation of optical signals in the C-band with CMOS-compatible voltages. The same platform can yield sizeable SHG when pumped by CW lasers in the C-band, which can also efficiently be modulated with similar voltages. Our approach achieves 0.07 reflectivity modulation with an oscillating voltage of $V_{pp} = 10 \text{ V}$ and a modulation efficiency of 0.015 V^{-1} , advancing the capabilities of metasurface-based EO modulators, especially in LNOI systems. The interdigitated electrodes design minimizes capacitance, pushing the bandwidth up to 800 MHz and allowing detectable modulation beyond 1 GHz ($f_{-6 \text{ dB}} = 1.4 \text{ GHz}$). A significant step forward with respect to the previously proposed free-space electro-optic devices is the SHG modulation induced by a static bias. Notably, we report the first experimental demonstration of electrically modulated SHG in subwavelength devices using CW

pumping [40]. In particular, we achieved a SHG intensity modulation exceeding one order of magnitude by applying $\Delta V_{EO} = 9$ V bias (i.e. with efficiency $\eta > 0.12$ V⁻¹), outperforming the linear counterpart. These results emphasize the value of utilizing narrow linewidth resonances, such as quasi-BIC, in combination with narrowband lasers. These findings demonstrate the feasibility of high-efficiency electro-optic modulation of nonlinear signals driven by low-power CW lasers, establishing a key technological milestone in nanophotonics [40].

Methods

Sample fabrication. The sample is fabricated via electron-beam lithography using a hydrogen silsesquioxane (HSQ) resist followed by Argon ion etching via an Inductively Coupled Plasma Reactive Ion-Etching (ICP-RIE) process. The redeposited amorphous LiNbO₃ is removed by means of KOH. The tilted sidewalls ($\theta = 65^\circ$, see Figure 2c) resulting from the purely physical etching process have been considered in the structure design. After fixing the filling factor FF and target $\alpha = 0.2$, we account for fabrication imperfections by fabricating several samples with slightly different bar lateral sizes, D_1 and D_2 in steps of 10 nm, ranging from -20 nm to 20 nm. In such a way we compensate for deviations from the nominal α value. Interdigitated electrodes and interconnects (300 nm Au on 5 nm Cr), obtained via direct laser beam lithography followed by metal evaporation, are placed orthogonally to the nanobars (Figure 2a).

Experimental setup. A continuous-wave (CW) diode laser source (TOPTICA CTL-1500) provides tuneable excitation in the communication C band (1460 nm - 1570 nm), with relative accuracy of 10 pm and laser bandwidth < 1 kHz. The laser is coupled to free space by means of a polarization-maintaining fiber (Thorlabs, P1-1550PM-FC-5) and its polarization is controlled by a broadband half-wavelength retarder (Thorlabs, AHWP05M-1600). A non-polarizing 50:50 beam splitter separates the excitation from the detection line in an epi-reflection configuration. Dealing with high- Q resonances imposes additional restrictions on the illumination characteristics. The BIC Q factor becomes finite by breaking the translational symmetry along the direction parallel to the 1D crystal axis (y axis in Figure S2a), as explained in the main text. Using a focusing system produces a superposition of plane waves with k vectors limited by the corresponding numerical aperture, thus smearing the resonance Q . This effect is mitigated by a long-focus ($f = 40$ cm) cylindrical lens (Thorlabs, LJ1363RM-C) inserted in the excitation path, which produces an elliptical spot at the back aperture of the objective (Mitutoyo, M Plan Apo NIR HR 50X). Here, the beam is focused along y and collimated along z , resulting in a reduced filling of the objective NA _{y} . This produces reduced number of k_y in the objective front-focal plane while keeping a tight focusing in the direction orthogonal to the grating axis. The signal collected by the objective is spectrally separated by means of a dichroic mirror with cut-off wavelength at 950 nm (Thorlabs, DMLP950). The reflected fundamental signal is detected by a fast InGaAs detector (Menlo Systems, FPD610-FS-NIR). The SHG signal is further spectrally filtered by a combination of filters (long pass at 600 nm and short pass at 900 nm from Thorlabs) to get rid of possible THG and other spurious signals. It is then coupled to a dispersive spectrometer (Andor, Shamrock SR303i) through a multimode fiber and detected by an open-electrode CCD camera (Andor, Newton DU920-OE). The modulating voltage $V(t)$ is provided by an arbitrary waveform generator (GW Instek) and consists in a sinusoidal wave of the form $V(t) = V_{DC} + \frac{V_{pp}}{2} \sin(2\pi f_{mod} t)$. An ultrahigh-frequency lock-in amplifier (Zurich Instrument, UHFLI) is referenced by the same waveform generator and simultaneously detect the AC and DC component of the signal from the photodiode through a split BNC cable.

The high-frequency characterization has been performed with a vector-network analyzer (Keysight, P5004A) driving the sample through an optimized microwave cable (Thorlabs, KMM36). The reflected, modulated optical signal from the sample is coupled into a single-mode fiber and optically amplified by

an erbium-doped fiber amplifier (Lumibird CEFA – CHG50), to exploit the full dynamics of a fast, single-mode, unamplified photodetector (New Focus, 45 GHz Photodetector). The electrical signal from the photodetector is then sent to the port 2 of the VNA through another microwave cable for the computation of the S_{21} parameter defined in the text.

Numerical simulations. The metasurfaces linear spectra, the refractive index change induced by Pockels effect and the second-harmonic generation (SHG) presented in this article have all been simulated by Finite-Element Method (FEM) using COMSOL Multiphysics® 6.2. The translational invariance along z allows us to implement a 2D unit cell (see Figure 2c), reducing the computational workload. We set a periodicity $p = 800$ nm for the supercell, which includes two asymmetric nanowires (150 nm high on top of 450 nm LiNbO₃ film). The LiNbO₃ ordinary and extraordinary index dispersion are described via Sellmeier equation [41]. We take into account the tilted sidewalls resulting from fabrication with an angle of $\theta = 65^\circ$. The LiNbO₃ grating is placed on top of a SiO₂ layer ($h_{\text{sub}} = 2$ μm, $n_2 = 1.45$) and Si (semi-infinite, $n_3 = 3.69$ at 775 nm [42] and $n_3 = 3.48$ at 1550 nm [43]). Floquet periodic boundary conditions are defined at the unit cell lateral boundaries to mimic an infinitely extended periodic structure. The upper semi-infinite space is made by air ($n_1 = 1$). We implement a three-steps simulation:

1. The change in the refractive index is calculated within a static field interface, available in the AC/DC module. For this step we define a 3D unit cell to calculate the static electric field \mathbf{E}_{EO} subtended by in-plane electrodes spaced by 14 μm. The static voltage V_0 is applied to a 300 nm – height Electric Potential port (the one on the other side of the electrodes is set to ground). Thanks to the uniformity of \mathbf{E}_{EO} in the LiNbO₃ film, only the solution for the z component $E_{\text{EO},z}$ is used to calculate the modifications of the refractive index induced by the Pockels effect [12]:

$$\begin{cases} n_x(\lambda, x, y, z) \approx n_0(\lambda) - \frac{1}{2}r_{13}(\lambda)n_0^3(\lambda)E_{\text{EO},z}(x, y, z), \\ n_y(\lambda, x, y, z) \approx n_0(\lambda) - \frac{1}{2}r_{13}(\lambda)n_0^3(\lambda)E_{\text{EO},z}(x, y, z), \\ n_z(\lambda, x, y, z) \approx n_0(\lambda) - \frac{1}{2}r_{33}(\lambda)n_e^3(\lambda)E_{\text{EO},z}(x, y, z), \end{cases} \quad (1)$$

with $r_{13} = 10.3$ pm/V and $r_{33} = 34.1$ pm/V [16] for $\lambda = 1.32$ μm, assumed to be the same at 1550 nm [44], and $r_{13} = 11$ pm/V and $r_{33} = 36.7$ pm/V for λ in the visible range [16].

2. The linear reflectance is calculated with a scattered-field formulation of the frequency domain interface of the wave optics module. We exploit the invariance along z and model the 2D unit cell as described above. We model a plane-wave excitation coming from the top port, impinging at normal incidence and polarized along the z axis for TE simulations (i.e., orthogonal to the simulation plane). Top and bottom ports work also to absorb the reflected and transmitted light, thus mimicking infinite Si and air layers in the $-x$ and $+x$ directions, respectively. The Pockels effect is included by performing a static field simulation (step 1) and extracting the averaged field E_{EO} in the LiNbO₃ layer. The electric field is indeed homogeneous in any xy cross section with almost no variation along z far away from the electrodes. Therefore, we know the LiNbO₃ refractive index change for any given input voltages V_0 with Equation 1.
3. SHG is calculated in a full-field, frequency domain formulation at twice the fundamental frequency. Under the hypothesis of undepleted pump, we use the solution of the optical electric field obtained from step 2 as fundamental field $E_i(\omega)$ for the computation of the nonlinear current density $\mathbf{J}(2\omega) = -2i\omega\mathbf{P}^{(2)}(2\omega)$. The nonlinear polarization $\mathbf{P}^{(2)}(2\omega)$ takes the form:

$$\begin{bmatrix} P_x^{(2)}(2\omega) \\ P_y^{(2)}(2\omega) \\ P_z^{(2)}(2\omega) \end{bmatrix} = 2\epsilon_0 \begin{bmatrix} 2d_{31}E_x(\omega)E_z(\omega) - 2d_{22}E_x(\omega)E_y(\omega) \\ -d_{22}E_x(\omega)^2 + d_{22}E_y(\omega)^2 + 2d_{31}E_y(\omega)E_z(\omega) \\ d_{31}E_x(\omega)^2 + d_{31}E_y(\omega)^2 + d_{33}E_z(\omega)^2 \end{bmatrix}, \quad (2)$$

which simplifies into $P_z(2\omega) = 2\epsilon_0 d_{33} E_z(\omega)^2$. To calculate the power radiated in the upper space we compute the Poynting vector flux $\int \mathbf{\Pi} \cdot d\mathbf{l}$, through the top-port boundary, where $\mathbf{\Pi}$ is the time-averaged Poynting vector and $d\mathbf{l}$ the outgoing vector normal to the top port. Perfectly matched layers have also been added after the linear ports for the SH computation to prevent any back reflection into the simulation volume. The Pockels effect has been considered in both steps of the second-harmonic computation by modifying the refractive index of the LiNbO₃ according to Sellmeier equations. In the case of the SH simulations, we took the values of the electro-optic coefficients measured at 632.8 nm [16]. As for the fundamental step, we used the average value of the static field in LiNbO₃ to compute the change of the refractive index. Also, the second order nonlinear coefficients d_{ij} are unknown at 1.5 μm . We thus used values measured for the fundamental wavelength at 1.313 μm ($d_{31} = -4.3$ pm/V, $d_{33} = -27$ pm/V)[45], while $d_{22} = 2.1$ pm/V [46].

Bibliography

- [1] S. A. Schulz *et al.*, “Roadmap on photonic metasurfaces,” *Appl Phys Lett*, vol. 124, no. 26, Jun. 2024, doi: 10.1063/5.0204694.
- [2] E. Mikheeva, C. Kyrou, F. Bentata, S. Khadir, S. Cuffe, and P. Genevet, “Space and Time Modulations of Light with Metasurfaces: Recent Progress and Future Prospects,” *ACS Photonics*, vol. 9, no. 5, pp. 1458–1482, May 2022, doi: 10.1021/acsp Photonics.1c01833.
- [3] S.-Q. Li, X. Xu, R. Maruthiyodan Veetil, V. Valuckas, R. Paniagua-Domínguez, and A. I. Kuznetsov, “Phase-only transmissive spatial light modulator based on tunable dielectric metasurface,” *Science (1979)*, vol. 364, no. 6445, pp. 1087–1090, Jun. 2019, doi: 10.1126/science.aaw6747.
- [4] Q. Wang *et al.*, “Optically reconfigurable metasurfaces and photonic devices based on phase change materials,” *Nat Photonics*, vol. 10, no. 1, pp. 60–65, Dec. 2015, doi: 10.1038/nphoton.2015.247.
- [5] K. Zangeneh Kamali *et al.*, “Electrically programmable solid-state metasurfaces via flash localised heating,” *Light Sci Appl*, vol. 12, no. 1, p. 40, Feb. 2023, doi: 10.1038/s41377-023-01078-6.
- [6] M. Celebrano *et al.*, “Optical tuning of dielectric nanoantennas for thermo-optically reconfigurable nonlinear metasurfaces,” *Opt Lett*, vol. 46, no. 10, p. 2453, May 2021, doi: 10.1364/OL.420790.
- [7] J. Sisler, P. Thureja, M. Y. Grajower, R. Sokhoyan, I. Huang, and H. A. Atwater, “Electrically tunable space–time metasurfaces at optical frequencies,” *Nat Nanotechnol*, Jul. 2024, doi: 10.1038/s41565-024-01728-9.
- [8] I.-C. Benea-Chelmus *et al.*, “Gigahertz free-space electro-optic modulators based on Mie resonances,” *Nat Commun*, vol. 13, no. 1, Jun. 2022, doi: 10.1038/s41467-022-30451-z.
- [9] S. Han *et al.*, “All-Dielectric Active Terahertz Photonics Driven by Bound States in the Continuum,” *Advanced Materials*, vol. 31, no. 37, Sep. 2019, doi: 10.1002/adma.201901921.
- [10] E. A. A. Pogna *et al.*, “Ultrafast, All Optically Reconfigurable, Nonlinear Nanoantenna,” *ACS Nano*, vol. 15, no. 7, pp. 11150–11157, Jul. 2021, doi: 10.1021/acsnano.1c03386.
- [11] A. Di Francescantonio *et al.*, “All-optical free-space routing of upconverted light by metasurfaces via nonlinear interferometry,” *Nat Nanotechnol*, vol. 19, no. 3, pp. 298–305, Mar. 2024, doi: 10.1038/s41565-023-01549-2.
- [12] R. W. Boyd, “Chapter 11 - The Electrooptic and Photorefractive Effects,” in *Nonlinear Optics (Third Edition)*, Third Edition., R. W. Boyd, Ed., Burlington: Academic Press, 2008, pp. 511–541. doi: <https://doi.org/10.1016/B978-0-12-369470-6.00011-3>.
- [13] A. J. Mercante, P. Yao, S. Shi, G. Schneider, J. Murakowski, and D. W. Prather, “110 GHz CMOS compatible thin film LiNbO₃ modulator on silicon,” *Opt Express*, vol. 24, no. 14, p. 15590, Jul. 2016, doi: 10.1364/OE.24.015590.
- [14] C. Wang *et al.*, “Integrated lithium niobate electro-optic modulators operating at CMOS-compatible voltages,” *Nature*, vol. 562, no. 7725, pp. 101–104, Oct. 2018, doi: 10.1038/s41586-018-0551-y.
- [15] A. Boes *et al.*, “Lithium niobate photonics: Unlocking the electromagnetic spectrum,” *Science (1979)*, vol. 379, no. 6627, Jan. 2023, doi: 10.1126/science.abj4396.

- [16] R. J. Holmes, Y. S. Kim, C. D. Brandle, and D. M. Smyth, "Evaluation of crystals of LiNbO₃ doped with MgO or TiO₂ for electrooptic devices," *Ferroelectrics*, vol. 51, no. 1, pp. 41–45, Nov. 1983, doi: 10.1080/00150198308009051.
- [17] D. A. Roberts, "Simplified characterization of uniaxial and biaxial nonlinear optical crystals: a plea for standardization of nomenclature and conventions," *IEEE J Quantum Electron*, vol. 28, no. 10, pp. 2057–2074, 1992, doi: 10.1109/3.159516.
- [18] M. Zhang, C. Wang, P. Kharel, D. Zhu, and M. Lončar, "Integrated lithium niobate electro-optic modulators: when performance meets scalability," *Optica*, vol. 8, no. 5, p. 652, May 2021, doi: 10.1364/OPTICA.415762.
- [19] A. Fedotova *et al.*, "Lithium Niobate Meta-Optics," *ACS Photonics*, vol. 9, no. 12, pp. 3745–3763, Nov. 2022, doi: 10.1021/acsp Photonics.2c00835.
- [20] M. Burla *et al.*, "500 GHz plasmonic Mach-Zehnder modulator enabling sub-THz microwave photonics," *APL Photonics*, vol. 4, no. 5, May 2019, doi: 10.1063/1.5086868.
- [21] D. Renaud *et al.*, "Sub-1 Volt and high-bandwidth visible to near-infrared electro-optic modulators," *Nat Commun*, vol. 14, no. 1, p. 1496, Mar. 2023, doi: 10.1038/s41467-023-36870-w.
- [22] H. C. Weigand, Ü.-L. Talts, A.-L. Vieli, V. V Vogler-Neuling, A. Nardi, and R. Grange, "Nanoimprinting Solution-Derived Barium Titanate for Electro-Optic Metasurfaces," *Nano Lett.*, vol. 24, no. 18, pp. 5536–5542, Apr. 2024, doi: 10.1021/acs.nanolett.4c00711.
- [23] S. Abel *et al.*, "A strong electro-optically active lead-free ferroelectric integrated on silicon," *Nat Commun*, vol. 4, no. 1, p. 1671, Apr. 2013, doi: 10.1038/ncomms2695.
- [24] W. Jin *et al.*, "Benzocyclobutene barrier layer for suppressing conductance in nonlinear optical devices during electric field poling," *Appl Phys Lett*, vol. 104, no. 24, Jun. 2014, doi: 10.1063/1.4884829.
- [25] H. Weigand *et al.*, "Enhanced Electro-Optic Modulation in Resonant Metasurfaces of Lithium Niobate," *ACS Photonics*, vol. 8, no. 10, pp. 3004–3009, Sep. 2021, doi: 10.1021/acsp Photonics.1c00935.
- [26] A. Weiss *et al.*, "Tunable Metasurface Using Thin-Film Lithium Niobate in the Telecom Regime," *ACS Photonics*, vol. 9, no. 2, pp. 605–612, Jan. 2022, doi: 10.1021/acsp Photonics.1c01582.
- [27] X. Chen *et al.*, "High quality factor resonant metasurface with etchless lithium niobate," *Opt Laser Technol*, vol. 161, p. 109163, Jun. 2023, doi: 10.1016/j.optlastec.2023.109163.
- [28] B. Gao, M. Ren, W. Wu, W. Cai, and J. Xu, "Electro-optic lithium niobate metasurfaces," *Science China*, vol. 64, no. 4, Feb. 2021, doi: 10.1007/s11433-021-1668-y.
- [29] Y. Ju *et al.*, "The electro-optic spatial light modulator of lithium niobate metasurface based on plasmonic quasi-bound states in the continuum," *Nanoscale*, vol. 15, no. 34, pp. 13965–13970, 2023, doi: 10.1039/D3NR02278A.
- [30] F. Ren *et al.*, "Surface-normal plasmonic modulator using sub-wavelength metal grating on electro-optic polymer thin film," *Opt Commun*, vol. 352, pp. 116–120, Oct. 2015, doi: 10.1016/j.optcom.2015.04.058.

- [31] A. Sabatti *et al.*, “Extremely high extinction ratio electro-optic modulator via frequency upconversion to visible wavelengths,” *Opt Lett*, vol. 49, no. 14, p. 3870, Jul. 2024, doi: 10.1364/OL.525733.
- [32] L. Huang *et al.*, “Ultrahigh-Q guided mode resonances in an All-dielectric metasurface,” *Nat Commun*, vol. 14, no. 1, Jun. 2023, doi: 10.1038/s41467-023-39227-5.
- [33] K. Sun *et al.*, “Infinite-Q guided modes radiate in the continuum,” *Phys Rev B*, vol. 107, no. 11, p. 115415, Mar. 2023, doi: 10.1103/PhysRevB.107.115415.
- [34] L. Huang *et al.*, “Ultrahigh-Q guided mode resonances in an All-dielectric metasurface,” *Nat Commun*, vol. 14, no. 1, Jun. 2023, doi: 10.1038/s41467-023-39227-5.
- [35] M. G. Moharam and T. K. Gaylord, “Rigorous coupled-wave analysis of planar-grating diffraction,” *J. Opt. Soc. Am.*, vol. 71, no. 7, p. 811, Jul. 1981, doi: 10.1364/josa.71.000811.
- [36] K. Koshelev, Y. Tang, K. Li, D.-Y. Choi, G. Li, and Y. Kivshar, “Nonlinear Metasurfaces Governed by Bound States in the Continuum,” *ACS Photonics*, vol. 6, no. 7, pp. 1639–1644, Jun. 2019, doi: 10.1021/acsp Photonics.9b00700.
- [37] F. Kaufmann, G. Finco, A. Maeder, and R. Grange, “Redeposition-free inductively-coupled plasma etching of lithium niobate for integrated photonics,” *Nanophotonics*, vol. 12, no. 8, pp. 1601–1611, Jan. 2023, doi: 10.1515/nanoph-2022-0676.
- [38] U. Fano, “Effects of Configuration Interaction on Intensities and Phase Shifts,” *Physical Review*, vol. 124, no. 6, pp. 1866–1878, Dec. 1961, doi: 10.1103/PhysRev.124.1866.
- [39] Z. He *et al.*, “Electro-optically Modulated Nonlinear Metasurfaces,” *Nano Lett*, vol. 24, no. 45, pp. 14215–14221, Nov. 2024, doi: 10.1021/acs.nanolett.4c03369.
- [40] A. P. Anthur *et al.*, “Continuous Wave Second Harmonic Generation Enabled by Quasi-Bound-States in the Continuum on Gallium Phosphide Metasurfaces,” *Nano Lett*, vol. 20, no. 12, pp. 8745–8751, Nov. 2020, doi: 10.1021/acs.nanolett.0c03601.
- [41] D. E. Zelmon, D. L. Small, and D. Jundt, “Infrared corrected Sellmeier coefficients for congruently grown lithium niobate and 5 mol% magnesium oxide –doped lithium niobate,” *Journal of the Optical Society of America B*, vol. 14, no. 12, p. 3319, Dec. 1997, doi: 10.1364/JOSAB.14.003319.
- [42] C. Schinke *et al.*, “Uncertainty analysis for the coefficient of band-to-band absorption of crystalline silicon,” *AIP Adv*, vol. 5, no. 6, Jun. 2015, doi: 10.1063/1.4923379.
- [43] C. D. Salzberg and J. J. Villa, “Infrared Refractive Indexes of Silicon Germanium and Modified Selenium Glass*,” *J Opt Soc Am*, vol. 47, no. 3, p. 244, Mar. 1957, doi: 10.1364/JOSA.47.000244.
- [44] J. L. Casson *et al.*, “Electro-optic coefficients of lithium tantalate at near-infrared wavelengths,” *Journal of the Optical Society of America B*, vol. 21, no. 11, p. 1948, Nov. 2004, doi: 10.1364/JOSAB.21.001948.
- [45] I. Shoji, T. Kondo, A. Kitamoto, M. Shirane, and R. Ito, “Absolute scale of second-order nonlinear-optical coefficients,” *Journal of the Optical Society of America B*, vol. 14, no. 9, p. 2268, Sep. 1997, doi: 10.1364/JOSAB.14.002268.
- [46] M. J. Weber, *Handbook of Optical Materials*. CRC Press, 2018. doi: 10.1201/9781315219615.